Journal of Science and Technology in Civil Engineering, HUCE, 2024, 18 (3): 30–47

A MITC3+ ELEMENT IMPROVED BY EDGE-BASED SMOOTHED STRAINS FOR FREE VIBRATION AND BUCKLING ANALYSES OF POROUS PLATES BASED ON THE FIRST-ORDER SHEAR DEFORMATION THEORY

Binh Le-Phuong[a], Thanh Chau-Dinh[a,*]

[a]*Faculty of Civil Engineering, Ho Chi Minh City University of Technology and Education, No. 1 Vo Van Ngan Street, Thu Duc City, Ho Chi Minh City, Vietnam*

Article history:
Received 09/4/2024, Revised 13/5/2024, Accepted 07/6/2024

Abstract

This paper presents the free vibration and critical buckling analyses of porous plates based on the first-order shear deformation theory by the proposed three-node triangular element. The bending strain fields of the suggested element are enriched by the bubble node located at the centroid of the triangular element. The shear-locking phenomenon is eliminated by the independent interpolations of the transverse shear strains following the MITC3+ technique. The edge-based smoothed (ES) strain method is employed to improve the in-plane strain fields. The influence of the porosity distributions, length-to-thickness ratios, porous coefficient, and boundary conditions on the free vibration and critical buckling load of the porous plates are evaluated through several numerical examples by the proposed element, namely ES-MITC3+ element. The obtained results are compared with other references to perform the efficiency of the proposed element.

Keywords: free vibration, buckling load; porous plate; first-order shear deformation; edge-based smoothed strain; MITC3+.

https://doi.org/10.31814/stce.huce2024-18(3)-03

1. Introduction

Porous material has an interconnected network of pores and must be specifically designed to yield the optimization of the material's performance. They are usually all around us and have multiple uses in different fields, including vibration damping, thermal insulation and sound absorption [1]. Foams or porous materials with a cellular structure have many special combinations of mechanical and physical properties, such as low specific weight high stiffness, excellent sound and thermal insulators [2]. Therefore, structures that are made of porous materials or porous-cellular materials have increasingly become popular in many fields, such as the civil engineering, automotive, aerospace industry and so on because of their excellent characteristics [3, 4]. In recent years, many studies on porous materials and related structures have been published.

A four-variable advanced plate theory was used by Barati et al. [5, 6] to investigate the natural vibration and instability of plate structures made of functionally graded (FG) materials with porosity. Wang and Zhang [7] studied the effects of three distinct porosity distributions throughout the thickness on the deflections and critical loadings of foam graphene plates. Wang and Zu [8] used both analytical and numerical techniques to analyze the nonlinear vibrations of functionally graded material plates with porosity Based on classical plate theory, Tran et al. [9] used an analytical method to study the geometrically nonlinear buckling and post-buckling behaviors of metal foam plates. Magnucka-Blandzi

*Corresponding author. *E-mail address:* chdthanh@hcmute.edu.vn (Chau-Dinh, T.)

[10] studied the critical buckling load of sandwich plates with a metal foam core, including the influence of porosity. Based on the first-order shear deformation theory (FSDT), Du et al. [11] investigated the free vibration of metal foam rectangular plates with three different types of porosity distribution along the thickness of the plates. Pham et al. [12] used a moving Kriging mesh-free method based on the higher-order shear deformation theory (HSDT) to study the free vibration and mechanical buckling of porous metal foam plates. The finite element method (FEM) was employed by Ebrahimi and Habibi [13] to examine the deflection and vibration of porous rectangular plates. Rezaei et al. [14] determined the natural frequencies of FG plates with porosities using the FSDT.

The literature mentioned above shows that numerous studies of plate structures made of porous materials have been conducted in recent years. The research is quite in-depth and extensive, revolving around many aspects related to the influence of the porosity coefficient, porosity distribution, and boundary conditions on the behaviors of structures. However, such recent improvements of the FEM as 3-node triangular elements [15] or smoothed FEM (SFEM) [16] have required further deep studies about the ability of developing to plate structures. Chau-Dinh et al. [17–19] investigated the isotropic, laminated composite or FG plates using the MITC3+ elements improved by employing the edge-based smoothed strains (ES) approach.

The objective of this paper focuses on the SFEM, based on the FSDT and the MITC3+ element [15] to develop a three-node triangular element plate for free vibration and critical buckling load analyses of plates made of porous materials. The bubble node is used to enrich the displacement approximations with a cubic shape function. This leads to the non-constant strain fields on each element. Consequently, the strain fields of the discrete structure are smoother than those given by the other conventional three-node triangular elements. The proposed ES-MITC3+ plate finite element can be used to analyze both thick and thin plates by using the independent interpolations of the transverse shear strains to remove the shear-locking phenomenon. In addition, the suggested ES-MITC3+ plate element is also used to evaluate the influence of the length-to-thickness ratios, porosity coefficient, and boundary conditions on the free natural frequencies and critical buckling load of the porous plates with three different porosity distributions across the thick plate.

In the next section, the formula of the ES-MITC3+ plate finite element for the free vibration and mechanical buckling analyses of porous plates is built. The proposed element's convergence, accuracy, and efficiency are presented in Section 3 through vibration and mechanical buckling analyses of several porous plates. Finally, some essential conclusions will be drawn in the last section.

2. Formulation of the ES-MITC3+ plate element for the free vibration and buckling analyses of porous plates

2.1. Three distinct types of porosity distributions

This work examines porous plates with three distinct porosity distribution types through the plate thickness t, including the uniform distribution (Type I), symmetric distribution (Type II) and asymmetric distribution (Type III) as illustrated in Fig. 1 The following expressions represent the variation of the mass density $\rho(z)$, shear modulus $G(z)$, and Young's modulus $E(z)$ along the z-direction of the plate thickness [11, 12].

- Type I:

$$\begin{cases} E(z) = E_1\,(1 - e_0\beta) \\ G(z) = G_1\,(1 - e_0\beta) \\ \rho(z) = \rho_1\left(1 - \sqrt{1 - e_0\beta}\right) \\ \beta = \dfrac{1}{e_0} - \dfrac{1}{e_0}\left(\dfrac{2}{\pi}\sqrt{1 - e_0} - \dfrac{2}{\pi} + 1\right)^2 \end{cases} \tag{1}$$

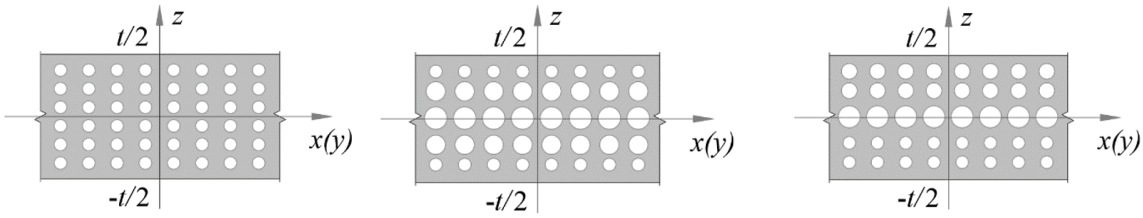

(a) Uniform distribution (Type I) (b) Symmetric distribution (Type II) (c) Asymmetric distribution (Type III)

Figure 1. Three typical kinds of the porosity distribution

- Type II:

$$\begin{cases} E(z) = E_1\left[1 - e_0\cos\left(\dfrac{\pi z}{t}\right)\right] \\ G(z) = G_1\left[1 - e_0\cos\left(\dfrac{\pi z}{t}\right)\right] \\ \rho(z) = \rho_1\left[1 - e_m\cos\left(\dfrac{\pi z}{t}\right)\right] \end{cases} \tag{2}$$

- Type III:

$$\begin{cases} E(z) = E_1\left[1 - e_0\cos\dfrac{\pi}{2}\left(\dfrac{z}{t} + \dfrac{1}{2}\right)\right] \\ G(z) = G_1\left[1 - e_0\cos\dfrac{\pi}{2}\left(\dfrac{z}{t} + \dfrac{1}{2}\right)\right] \\ \rho(z) = \rho_1\left[1 - e_m\cos\dfrac{\pi}{2}\left(\dfrac{z}{t} + \dfrac{1}{2}\right)\right] \end{cases} \tag{3}$$

where e_m and e_0 denote the porosity density coefficient and porosity coefficient, respectively. In addition, e_m can be computed by

$$e_m = 1 - \sqrt{1 - e_0} \tag{4}$$

In this study, the Poisson's ratio v is assumed to be constant [20].

2.2. Displacement approximations and strain fields of the MITC3+ element based on the FSDT

The displacements of a porous plate are determined by utilizing the first-order shear deformation theory as follows

$$\begin{aligned} u(x, y, z) &= u_0(x, y) + z\beta_x(x, y) \\ v(x, y, z) &= v_0(x, y) + z\beta_y(x, y) \\ w(x, y, z) &= w_0(x, y) \end{aligned} \tag{5}$$

where u_0, v_0, and w_0 denote the displacements of the middle plane in the x, y, and z directions, respectively; β_x and β_y represent the rotations of the middle plane about the y and x axes, respectively, as shown in Fig. 2.

Discretizing the middle plane of the porous plate into three-node triangular elements. The displacement fields of the middle plate are approximated by

$$u_0 = \sum_{I=1}^{4} N_I u_{0I}; \quad v_0 = \sum_{I=1}^{4} N_I v_{0I}; \quad w_0 = \sum_{I=1}^{4} N_I w_{0I}; \quad \beta_x = \sum_{I=1}^{4} N_I \theta_{yI}; \quad \beta_y = -\sum_{I=1}^{4} N_I \theta_{xI} \tag{6}$$

here, u_{0I}, v_{0I}, and w_{0I} are respectively the translational displacements of node I along the x, y, and z axes and notice that $w_{04} = 0$ to maintain the flat geometry of the element; θ_{xI} and θ_{yI} are the rotations

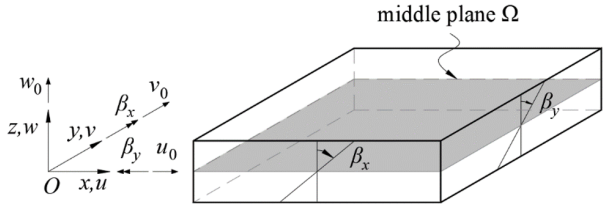

Figure 2. The porous plate's geometric characteristic symbols and coordinates

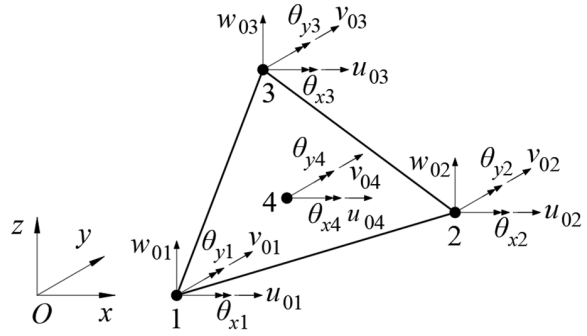

Figure 3. Positive signs of the degrees of freedom at the nodes of the three-node triangular element with a bubble node

of node I about the x and y axes, respectively; the positive signs of the nodal displacements are defined in Fig. 3; N_I are the cubic bubble interpolation functions expressed in the natural coordinates (ξ, η) by

$$\begin{aligned} N_1 &= 1-\xi-\eta-9\xi\eta(1-\xi-\eta); \quad N_2 = \xi-9\xi\eta(1-\xi-\eta) \\ N_3 &= \eta-9\xi\eta(1-\xi-\eta); \quad N_4 = 27\xi\eta(1-\xi-\eta) \end{aligned} \tag{7}$$

From the displacement approximations in Eq. (6), the strain fields of the element are derived in terms of the nodal displacements

$$\boldsymbol{\varepsilon} = \left\{ \begin{array}{c} \varepsilon_{xx} \\ \varepsilon_{yy} \\ \gamma_{xy} \end{array} \right\} = \underbrace{\left\{ \begin{array}{c} u_{0,x} \\ v_{0,y} \\ u_{0,y}+v_{0,x} \end{array} \right\}}_{\boldsymbol{\varepsilon}_m} + z \underbrace{\left\{ \begin{array}{c} \beta_{x,x} \\ \beta_{y,y} \\ \beta_{x,y}+\beta_{y,x} \end{array} \right\}}_{\boldsymbol{\varepsilon}_b} = \underbrace{\sum_{I=1}^{4} \mathbf{B}_m^I \mathbf{d}_I}_{\boldsymbol{\varepsilon}_m} + z \underbrace{\sum_{I=1}^{4} \mathbf{B}_b^I \mathbf{d}_I}_{\boldsymbol{\varepsilon}_b} \tag{8}$$

$$\boldsymbol{\gamma} = \left\{ \begin{array}{c} \gamma_{xz} \\ \gamma_{yz} \end{array} \right\} = \left\{ \begin{array}{c} w_{0,x}+\beta_x \\ w_{0,y}+\beta_y \end{array} \right\} = \sum_{I=1}^{4} \mathbf{B}_s^I \mathbf{d}_I \tag{9}$$

in which

$$\mathbf{B}_m^I = \left[\begin{array}{ccccc} N_{I,x} & 0 & 0 & 0 & 0 \\ 0 & N_{I,y} & 0 & 0 & 0 \\ N_{I,y} & N_{I,x} & 0 & 0 & 0 \end{array} \right]; \quad \mathbf{B}_b^I = \left[\begin{array}{ccccc} 0 & 0 & 0 & 0 & N_{I,x} \\ 0 & 0 & 0 & -N_{I,y} & 0 \\ 0 & 0 & 0 & -N_{I,x} & N_{I,y} \end{array} \right] \tag{10}$$

$$\mathbf{B}_s^I = \left[\begin{array}{ccccc} 0 & 0 & N_{I,x} & 0 & N_I \\ 0 & 0 & N_{I,y} & -N_I & 0 \end{array} \right] \tag{11}$$

with, $\mathbf{d}_I = \left[\begin{array}{ccccc} u_{0I} & v_{0I} & w_{0I} & \theta_{xI} & \theta_{yI} \end{array} \right]^T$ and $w_{04} = 0$.

Theoretically, as the thickness of the plate decreases, the transverse shear strains approach zero. Nevertheless, because the displacements estimated in Eq. (6) employ the C^0-type shape functions, the

approximations of the transverse shear strains cannot reach zero. It is called the shear-locking phenomenon. In this paper, the shear-locking phenomenon is eliminated by the independent interpolations of the transverse shear strains following the MITC3+ technique [15] as follows

$$\begin{cases} \hat{\gamma}_{\xi\varsigma} = \dfrac{2}{3}\left(\gamma^B_{\xi\varsigma} - \dfrac{1}{2}\gamma^B_{\eta\varsigma}\right) + \dfrac{1}{3}\left(\gamma^C_{\xi\varsigma} + \gamma^C_{\eta\varsigma}\right) + \dfrac{1}{3}\left[\left(\gamma^F_{\xi\varsigma} - \gamma^D_{\xi\varsigma}\right) - \left(\gamma^F_{\eta\varsigma} - \gamma^E_{\eta\varsigma}\right)\right](3\eta - 1) \\ \hat{\gamma}_{\eta\varsigma} = \dfrac{2}{3}\left(\gamma^A_{\eta\varsigma} - \dfrac{1}{2}\gamma^A_{\xi\varsigma}\right) + \dfrac{1}{3}\left(\gamma^C_{\xi\varsigma} + \gamma^C_{\eta\varsigma}\right) + \dfrac{1}{3}\left[\left(\gamma^F_{\xi\varsigma} - \gamma^D_{\xi\varsigma}\right) - \left(\gamma^F_{\eta\varsigma} - \gamma^E_{\eta\varsigma}\right)\right](1 - 3\xi) \end{cases} \tag{12}$$

wherein $\gamma^{(*)}_{\xi\varsigma}, \gamma^{(*)}_{\eta\varsigma}$ are the transverse shear strains in the natural coordinate system computed from Eq. (9) at the tying points A, B, C, D, E and F defined in Fig. 4.

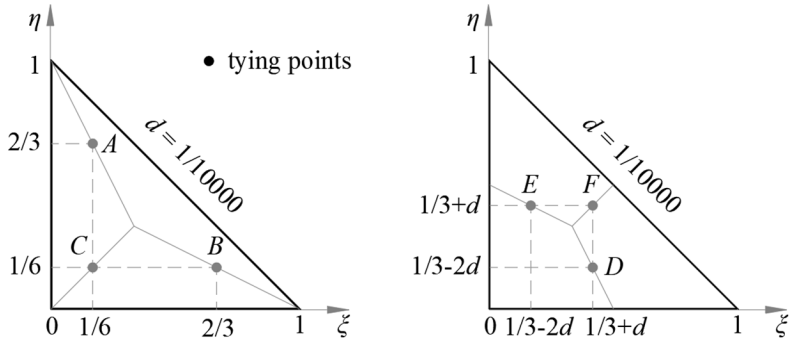

Figure 4. The tying points' coordinates in the natural coordinate system [15]

The MITC3+ transverse shear strains in Eq. (12) are described in terms of the nodal displacements by calculating the transverse shear strains in Eq. (9) at the tying points and substituting them into Eq. (12). As a result, we have

$$\hat{\boldsymbol{\gamma}}_s = \begin{Bmatrix} \hat{\gamma}_{xz} \\ \hat{\gamma}_{yz} \end{Bmatrix} = \sum_{I=1}^{4} \hat{\mathbf{B}}^I_s \mathbf{d}_I \tag{13}$$

2.3. Formulation of the ES-MITC3+ element for the porous plates based on the FSDT

The strain fields in standard FEM are determined on each element from the displacement approximations. Therefore, the three-node triangular MITC3+ plate finite elements do not display interelement continuity of the train fields. When the mesh is not adequately refined, the difference of the strain fields between adjacent elements becomes larger. To reduce this significant difference, Liu and Nguyen-Thoi [16] suggested the edge-based smoothed (ES) FEM to average the strain fields on domains determined by elements sharing common edges.

In this work, the in-plane strain fields of the MITC3+ components are smoothed using the ES-FEM to simulate the behavior of the porous plate employing FSDT-type theory. The in-plane strain fields are averaged across the smoothing domain Ω_s defined by the straight-line segments connecting the centroids of two adjacent elements and the two nodes of the common edge, as shown in Fig. 5(a).

Therefore, the strain fields provided in Eq. (8) are smoothed by

$$\begin{aligned} \tilde{\boldsymbol{\varepsilon}}_m &= \frac{1}{A_s}\int_{\Omega_s} \boldsymbol{\varepsilon}_m \mathrm{d}\Omega = \frac{1}{A_s}\int_{\Omega_s}\left(\sum_{I=1}^{4}\mathbf{B}^I_m\mathbf{d}_I\right)\mathrm{d}\Omega = \frac{1}{A_s}\sum_{I=1}^{4}\left(\int_{\Omega_s}\mathbf{B}^I_m\mathrm{d}\Omega\right)\mathbf{d}_I \\ \tilde{\boldsymbol{\varepsilon}}_b &= \frac{1}{A_s}\int_{\Omega_s} \boldsymbol{\varepsilon}_b \mathrm{d}\Omega = \frac{1}{A_s}\int_{\Omega_s}\left(\sum_{I=1}^{4}\mathbf{B}^I_b\mathbf{d}_I\right)\mathrm{d}\Omega = \frac{1}{A_s}\sum_{I=1}^{4}\left(\int_{\Omega_s}\mathbf{B}^I_b\mathrm{d}\Omega\right)\mathbf{d}_I \end{aligned} \tag{14}$$

in which, A_s is the area of the edge-based smoothing domain Ω_s.

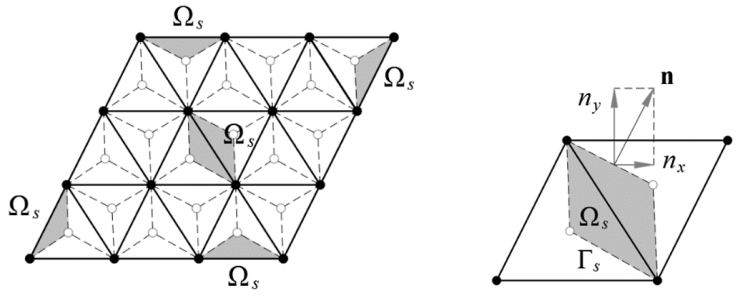

(a) Ω_s (b) $\mathbf{n}$

Figure 5. The edge-based smoothing domains Ω_s and vector $\mathbf{n}$ normal to the boundary Γ_s of the smoothing domain Ω_s

The surface integration of the gradient matrices in Eq. (14) is converted to the line integration using the divergence theorem as follows

$$\int_{\Omega_s} N_{I,x} \mathrm{d}\Omega = \int_{\Gamma_s} N_I n_x \mathrm{d}\Gamma; \quad \int_{\Omega_s} N_{I,y} \mathrm{d}\Omega = \int_{\Gamma_s} N_I n_y \mathrm{d}\Gamma \tag{15}$$

here, n_x and n_y are the components of the vector $\mathbf{n}$ normal the boundary Γ_s of the smoothing domain Ω_s as shown in Fig. 5(b).

The line integration in Eq. (15) is numerically evaluated by the two-point Gaussian quadrature method on each straight segment of the boundary Γ_s. Therefore,

$$\int_{\Gamma_s} N_I n_x \mathrm{d}\Gamma = \sum_{ed=1}^{N_{ed}} \sum_{qp=1}^{2} N_I^{qp} W_{qp} n_x^{ed}; \quad \int_{\Gamma_s} N_I n_y d\Gamma = \sum_{ed=1}^{N_{ed}} \sum_{qp=1}^{2} N_I^{qp} W_{qp} n_y^{ed} \tag{16}$$

where N_{ed} is the number of segments of Γ_s and N_I^{qp} are the value of the shape function N_I at the Gaussian quadrature point qp with the associated weights W_{qp}.

Denote $N_{Ix} = \sum_{ed=1}^{N_{ed}} \sum_{qp=1}^{2} N_I^{qp} W_{qp} n_x^{ed}; N_{Iy} = \sum_{ed=1}^{N_{ed}} \sum_{qp=1}^{2} N_I^{qp} W_{qp} n_y^{ed}$. We can express the surface integrations in Eq. (15) in terms of N_{Ix} and N_{Iy} as

$$\int_{\Omega_s} \mathbf{B}_m^I \mathrm{d}\Omega = \tilde{\mathbf{B}}_m^I = \begin{bmatrix} N_{Ix} & 0 & 0 & 0 & 0 \\ 0 & N_{Iy} & 0 & 0 & 0 \\ N_{Iy} & N_{Ix} & 0 & 0 & 0 \end{bmatrix}; \int_{\Omega_s} \mathbf{B}_b^I \mathrm{d}\Omega = \tilde{\mathbf{B}}_b^I = \begin{bmatrix} 0 & 0 & 0 & 0 & N_{Ix} \\ 0 & 0 & 0 & -N_{Iy} & 0 \\ 0 & 0 & 0 & -N_{Ix} & N_{Iy} \end{bmatrix} \tag{17}$$

Consequently, the relations between the smoothed strains and the nodal displacement in Eq. (14) are rewritten as

$$\tilde{\varepsilon}_m = \frac{1}{A_s} \sum_{I=1}^{4} \tilde{B}_m^I d_I; \quad \tilde{\varepsilon}_b = \frac{1}{A_s} \sum_{I=1}^{4} \tilde{B}_b^I d_I \tag{18}$$

Following the standard finite element procedure, substituting the relations between the smoothed strains and nodal displacements into the virtual work principle the discretized equations of the plate element Ω_e can be described as follows

$$\mathbf{m}_e \ddot{\mathbf{d}}_e + \left(\mathbf{k}_e - \mathbf{k}_g\right) \mathbf{d}_e = \mathbf{0} \tag{19}$$

in which, $\mathbf{d}_e$ is the element nodal displacements; $\mathbf{m}_e$, $\mathbf{k}_e$ and $\mathbf{k}_g$ are respectively the mass, stiffness, and geometric matrices of the ES-MITC3+ element determined by

$$\mathbf{m}_e^{IJ} = \int_{\Omega_e} \left(\mathbf{N}^I\right)^T \mathbf{m}\mathbf{N}^J \mathrm{d}\Omega \tag{20}$$

$$\begin{aligned}\mathbf{k}_e^{IJ} = &\int_{\Omega_e} \left(\tilde{\mathbf{B}}_m^I\right)^T \mathbf{A}\tilde{\mathbf{B}}_m^J \mathrm{d}\Omega + \int_{\Omega_e} \left(\tilde{\mathbf{B}}_b^I\right)^T \mathbf{B}\tilde{\mathbf{B}}_m^J \mathrm{d}\Omega + \int_{\Omega_e} \left(\tilde{\mathbf{B}}_m^I\right)^T \mathbf{B}\tilde{\mathbf{B}}_b^J \mathrm{d}\Omega \\ &+ \int_{\Omega_e} \left(\tilde{\mathbf{B}}_b^I\right)^T \mathbf{D}\tilde{\mathbf{B}}_b^J \mathrm{d}\Omega + \int_{\Omega_e} \left(\hat{\mathbf{B}}_s^I\right)^T \mathbf{D}_s\hat{\mathbf{B}}_s^J \mathrm{d}\Omega\end{aligned} \tag{21}$$

$$\mathbf{k}_g^{IJ} = \int_{\Omega_e} \left(\mathbf{B}_g^I\right)^T \mathbf{N}_0\mathbf{B}_g^J \mathrm{d}\Omega \tag{22}$$

with

$$\mathbf{m} = \begin{bmatrix} I_0 & 0 & 0 & I_1 & 0 \\ 0 & I_0 & 0 & 0 & I_1 \\ 0 & 0 & I_0 & 0 & 0 \\ I_1 & 0 & 0 & I_2 & 0 \\ 0 & I_1 & 0 & 0 & I_2 \end{bmatrix} \text{ and } (I_0, I_1, I_2) = \int_{-\frac{t}{2}}^{\frac{t}{2}} \rho(z)\left(1, z, z^2\right)\mathrm{d}z \tag{23}$$

$$\mathbf{N}^I = \begin{bmatrix} N_I & 0 & 0 & 0 & 0 \\ 0 & N_I & 0 & 0 & 0 \\ 0 & 0 & N_I & 0 & 0 \\ 0 & 0 & 0 & N_I & 0 \\ 0 & 0 & 0 & 0 & N_I \end{bmatrix} \tag{24}$$

$$\mathbf{A} = \bar{\boldsymbol{\nu}}_1 \int_{-\frac{t}{2}}^{\frac{t}{2}} E(z)\mathrm{d}z; \quad \mathbf{B} = \bar{\boldsymbol{\nu}}_1 \int_{-\frac{t}{2}}^{\frac{t}{2}} E(z)\, z\mathrm{d}z; \quad \mathbf{D} = \bar{\boldsymbol{\nu}}_1 \int_{-\frac{t}{2}}^{\frac{t}{2}} E(z) z^2 \mathrm{d}z \tag{25}$$

$$\mathbf{D}_s = \frac{5}{6}\frac{t^2}{t^2 + \alpha h_e^2}\bar{\boldsymbol{\nu}}_2 \int_{-\frac{t}{2}}^{\frac{t}{2}} E(z)\mathrm{d}z \tag{26}$$

and

$$\bar{\boldsymbol{\nu}}_1 = \begin{bmatrix} \frac{1}{1-\nu^2} & \frac{\nu}{1-\nu^2} & 0 \\ \frac{\nu}{1-\nu^2} & \frac{1}{1-\nu^2} & 0 \\ 0 & 0 & \frac{1-\nu}{2(1-\nu^2)} \end{bmatrix}; \quad \bar{\boldsymbol{\nu}}_2 = \begin{bmatrix} \frac{1}{2(1+\nu)} & 0 \\ 0 & \frac{1}{2(1+\nu)} \end{bmatrix} \tag{27}$$

$$\mathbf{B}_g^I = \begin{bmatrix} N_{I,x} & 0 & 0 & 0 & 0 \\ N_{I,y} & 0 & 0 & 0 & 0 \\ 0 & N_{I,x} & 0 & 0 & 0 \\ 0 & N_{I,y} & 0 & 0 & 0 \\ 0 & 0 & N_{I,x} & 0 & 0 \\ 0 & 0 & N_{I,y} & 0 & 0 \end{bmatrix}; \quad \mathbf{N}_0 = \begin{bmatrix} N_x & N_{xy} & 0 & 0 & 0 & 0 \\ N_{xy} & N_y & 0 & 0 & 0 & 0 \\ 0 & 0 & N_x & N_{xy} & 0 & 0 \\ 0 & 0 & N_{xy} & N_y & 0 & 0 \\ 0 & 0 & 0 & 0 & N_x & N_{xy} \\ 0 & 0 & 0 & 0 & N_{xy} & N_y \end{bmatrix} \tag{28}$$

In this study, the constitutive matrix of the transverse shear strains in Eq. (26) is stabilized by the modification factor in which h_e is the longest length of the element's edges and $\alpha = 0.1$ [21].

The natural frequencies ω and mode shape $\boldsymbol{\phi}$ of the plate's free vibration are determined by solving the following equations

$$\left(\mathbf{K} - \omega^2\mathbf{M}\right)\boldsymbol{\phi} = 0 \tag{29}$$

For mechanical buckling analyses, the critical buckling load factor λ is obtained by the below equations

$$\left(\mathbf{K} - \lambda\mathbf{K}_g\right)\mathbf{d} = 0 \tag{30}$$

where **M, K**, and $\mathbf{K}_g$ are respectively the global mass, stiffness and geometric matrices of the plate assembled from the mass, stiffness, and geometric matrices of the ES-MITC3+ elements given in Eqs. (20), (21), (22).

3. Numerical results

In this section, the proposed ES-MITC3+ finite element will be used to analyze free vibration and buckling responses of several square plates made of the three different kinds of porosity distributions. The obtained results are compared with other references to evaluate the efficiency of the proposed element The boundary conditions of plate are investigated as follows:

- CCCC designates the clamped condition on all edges.
- SSSS refers to the simply supported condition on all edges.
- SCSS indicates the clamped condition on one edge and the simply supported ones on the other edges.

3.1. Free vibration analysis

a. Porous metal foam square plate

The first numerical example focuses on a porous metal foam square plate. The plate has the length of edges a and thickness t as shown in Fig. 6. The material properties are $E_1 = 200$ GPa, $\nu = 0.33$, $\rho_1 = 7850$ kg/m^3.

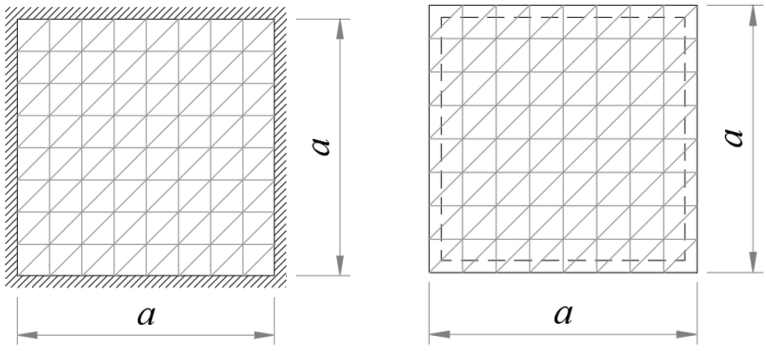

(a) CCCC (b) SSSS

Figure 6. Geometry of the square plates with the (a) CCCC and (b) SSSS boundaries; and the regularly triangular meshes with $N = 8$

To investigate the convergence rate of the ES-MITC3+ plate element when used to determine the free vibration of the plate under different boundary conditions, including the CCCC and SSSS boundaries the regular meshes of $N = 8$, 12, 20, and 24 in which N is the number of elements on each edge are employed. Fig. 6 demonstrates the mesh of $N = 8$. In this example, the normalized natural frequency $\overline{\Omega} = 100\omega t\,(\rho_1/E_1)^{1/2}$ for the five lowest modes of the plate is considered.

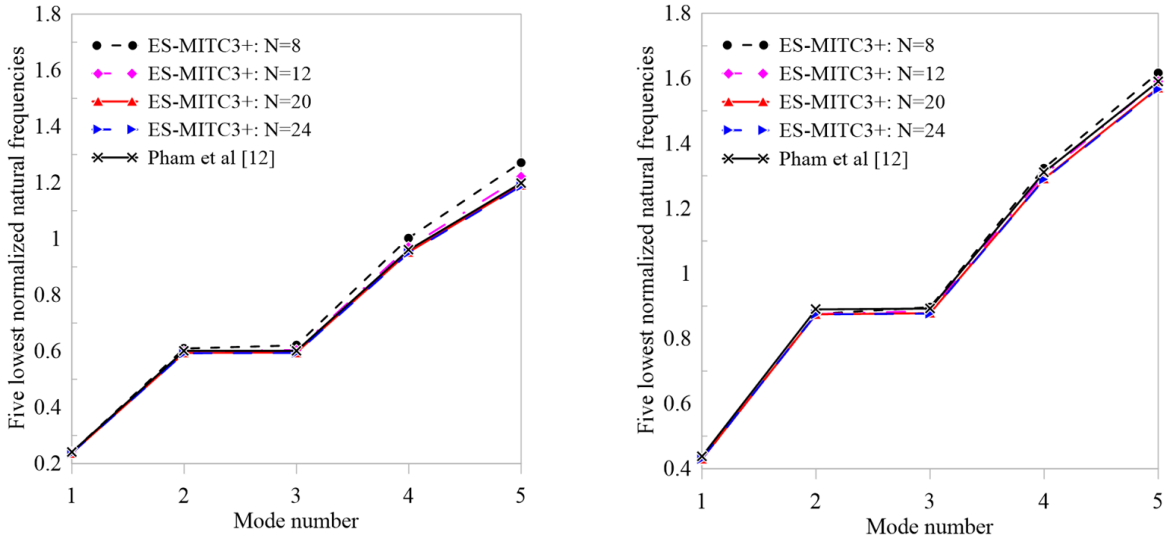

(a) SSSS (b) CCCC

Figure 7. The five lowest normalized natural frequencies of the symmetric porous metal foam square plate when element sizes in the mesh decrease (a/t = 50, e_0 = 0.1)

The five lowest normalized frequencies of the symmetric porous plate given by the ES-MITC3+ element versus the various element sizes are plotted in Fig. 7(a) and Fig. 7(b) for the SSSS and CCCC boundary conditions, respectively. The results well converge to those of Pham et al. [12] when increasing the number of element on each edge. The best natural frequencies provided by the ES-MITC3+ element yield when the mesh of N = 24 is used. With the mesh of N = 24, the three lowest normalized frequencies of the metal foam square plates made of varying porosity distribution types given by the ES-MITC3+ elements are presented in Table 1 and Table 2. In comparison with Pham et al. [12], the obtained results are in excellent agreement.

Table 1. Three lowest normalized natural frequencies of the porous metal foam square plate with the SSSS boundary condition on the edges (a/t =10, e_0 = 0.1)

Type	Mode	Pham et al. [12]	ES-MITC3+	% Relative error
Type I	1	5.7276	5.6940	0.59
	2	13.6513	13.7288	0.57
	3	13.6566	13.7569	0.73
Type II	1	5.8051	5.7340	1.22
	2	13.8138	13.6943	0.87
	3	13.8191	13.7239	0.69
Type III	1	5.7421	5.6698	1.26
	2	13.6821	13.5531	0.94
	3	13.6874	13.5824	0.77

Table 2. Three lowest normalized natural frequencies of the porous metal foam square plate with the CCCC boundary condition on the edges (a/t =10, e_0 = 0.1)

Type	Mode	Pham et al. [12]	ES-MITC3+	% Relative error
Type I	1	9.7405	9.7096	0.32
	2	18.5511	18.6849	0.72
	3	18.6119	18.7342	0.66
Type II	1	9.8482	9.7625	0.87
	2	18.7193	18.6159	0.55
	3	18.7804	18.6706	0.58
Type III	1	9.7611	9.6662	0.97
	2	18.5839	18.4536	0.70
	3	18.6447	18.5078	0.73

b. Porous-cellular aluminum square plate

The frequency analysis of a cellular aluminum square plate of the edge a and thickness t with asymmetric porosity distribution is presented in this example. The material properties of the plates are G_1 = 26.923 GPa, ν = 0.3, $E_1 = 2G_1(1+\nu)$ and ρ_1 = 2707 kg/m^3. The normalized natural frequency of the plate is computed by $\varpi = \omega t(\rho_1/E_1)^{1/2}$.

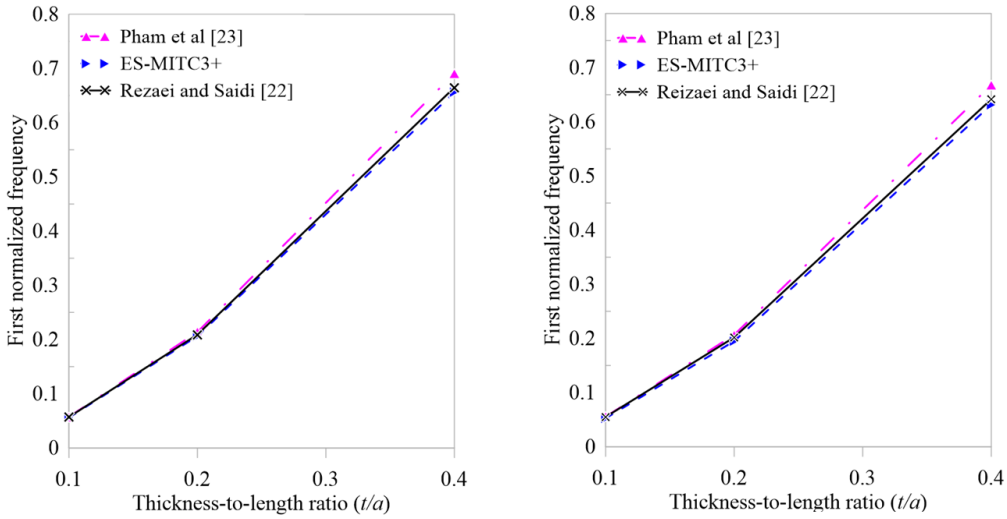

(a) e_0 = 0.1 (b) e_0 = 0.3

Figure 8. Influence of thickness-to-length ratios on the first normalized frequency of the simply supported cellular aluminum square plate with asymmetric porosity distribution

The first normalized frequencies of the SSSS cellular aluminum square plates with asymmetric porosity distribution provided by the ES-MITC3+ element using the mesh of N = 24 are demonstrated in Fig. 8. With the thickness-to-length ratios ranging from 0.1 to 0.4 and the porosity coefficients of 0.1 and 0.3, the results obtained by the ES-MITC3+ element are similar to those of Rezaei and Saidi [22] and better than those of Pham et al. [23]. The influence of the thickness-to-length ratios and

porous coefficients on the first normalized frequency of the asymmetric porous cellular aluminum square plate with the SSSS and SCSS boundary conditions is shown in Fig. 9. The thicker the plate is, the lower the natural frequency is when the porous coefficients increase. Fig. 9 also shows the accuracy of the proposed ES-MITC3+ element in comparison with Rezaei and Saidi [22].

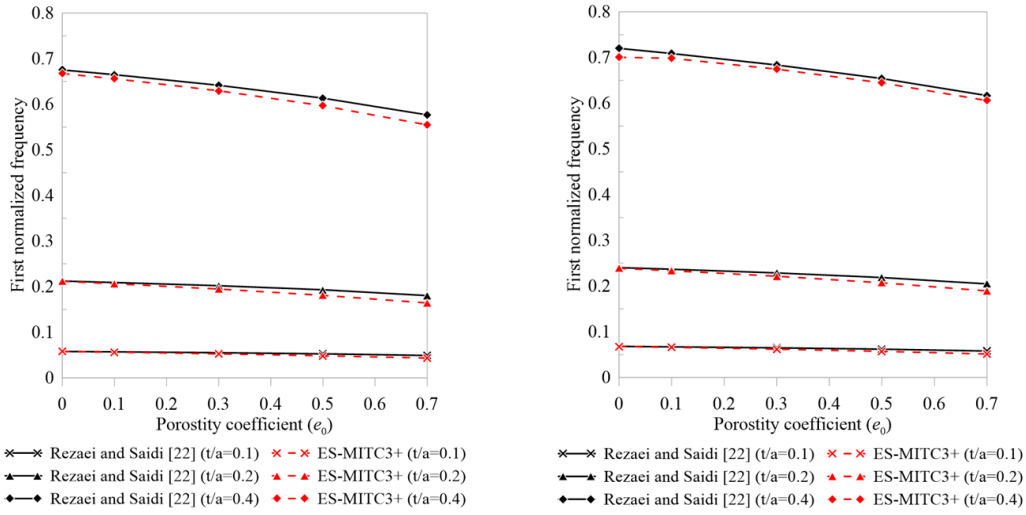

(a) SSSS (b) SCSS

Figure 9. First normalized frequency of the asymmetric porous cellular aluminum square plate having the various boundary conditions, porosity coefficients and thickness-to-length ratios

c. Square metal foam plate with a circular hole

A square plate has the length of edges $a = 1$, thickness t and contains a circular hole with the diameter $d = 0.5$ as shown in Fig. 10. All edges of the plate are clamped or simply supported. The plate is made of porous foam material with different porosity distributions. The material properties are $E_1 = 200$ GPa, $\nu = 0.33$ and $\rho_1 = 7850$ kg/m^3. To compare with reference solutions [12], the normalized natural frequencies of the plate are defined by $\overline{\Omega} = 100\omega t\,(\rho_1/E_1)^{1/2}$.

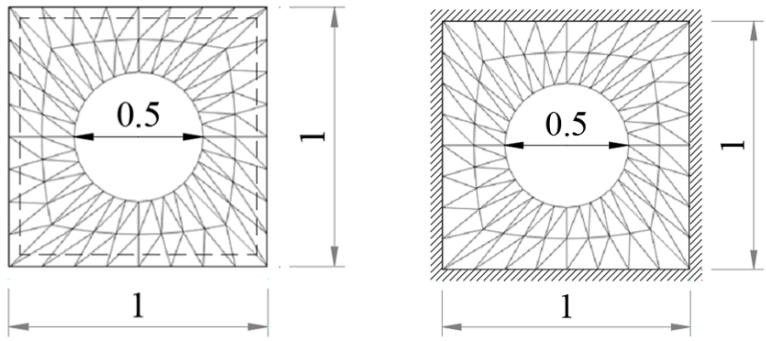

(a) SSSS (b) CCCC

Figure 10. Geometry of the (a) SSSS and (b) CCCC plates with a circular hole and meshes with $N = 8$

The plate is discretized by triangular meshes with the number of elements on each edge N = 8, 12, 16, 20 and 24. Fig. 10 shows the mesh with $N = 8$. Fig. 11 compares the first normalized

frequency of the metal foam plate with $a/t = 10$ and uniformly distributed porosity $e_0 = 0.1$ obtained by the proposed ES-MITC3+ element and the other three-node triangular MITC3 and ES-MITC3 elements when using different meshes. It shows the enhancement of the ES-MITC3+ element over the MITC3 and ES-MITC3 elements in comparison with Pham et al. [12] because of the displacement approximation enriched by the cubic shape function at the bubble node.

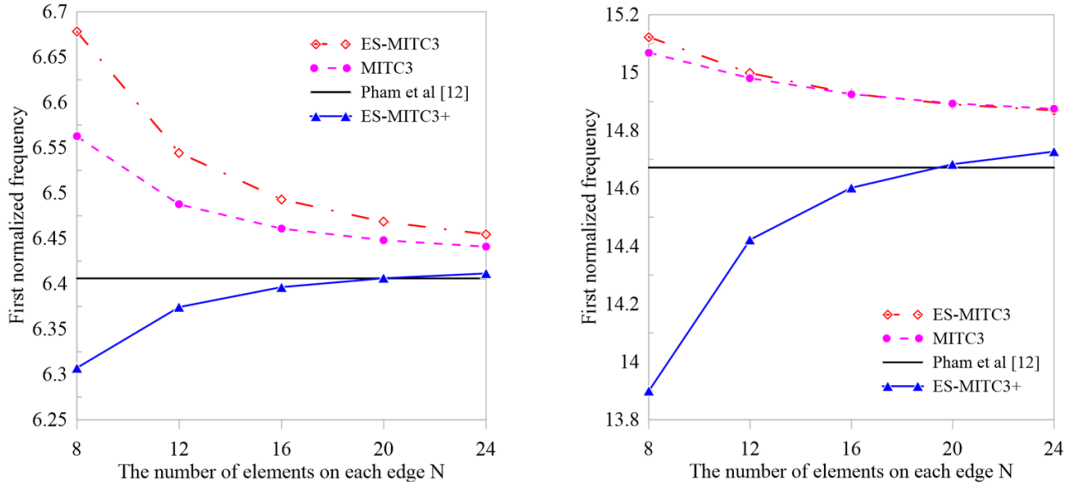

(a) SSSS (b) CCCC

Figure 11. Convergence of the first normalized frequency of the square plate with a circular hole made of uniformly porous distributed metal foam ($a/t = 10$, $e_0 = 0.1$) given by various three-node triangular elements when increasing the number of elements on each edge N

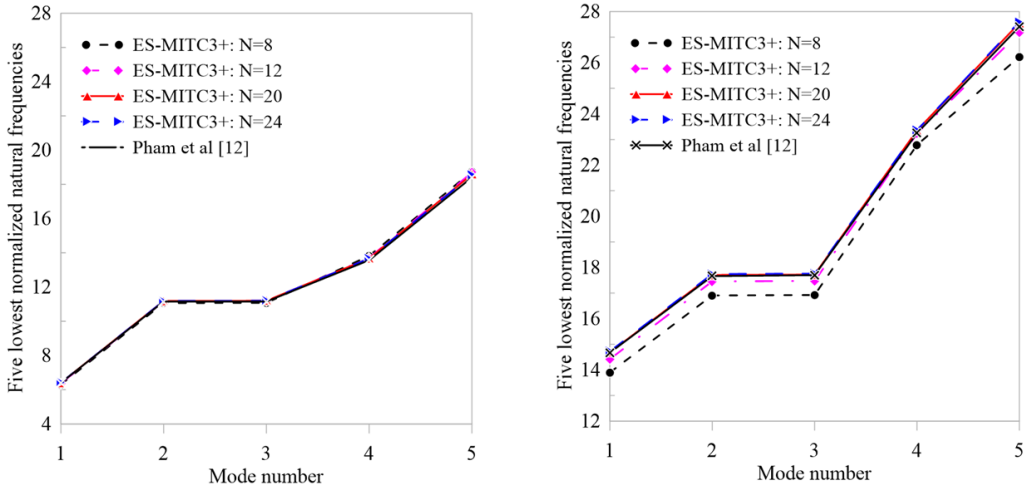

(a) SSSS (b) CCCC

Figure 12. The five lowest normalized natural frequencies of the porous metal foam square plate with a circular hole corresponding to uniform porosity distribution when decreasing element sizes in the mesh ($a/t = 10$, $e_0 = 0.1$)

When using the gradually dense meshes, the five lowest normalized frequencies $\overline{\Omega}$ of the uniformly distributed porous metal foam square plate given by the ES-MITC3+ element converge to the

reference results [12] as plotted in Fig. 12. Employing the convergent mesh of $N = 24$, the three lowest normalized frequencies of the square plate with the circular hole provided by the ES-MITC3+ element for the different types of the porosity distributions with the coefficients $e_0 = 0.1$ and 0.2, and the length-to-thickness ratios $a/t = 10$ and 30 are presented in Table 3, Table 4 for the SSSS boundary conditions and in Table 5, Table 6 for the CCCC boundary conditions. The results in tables indicate the accuracy of the suggested ES-MITC3+ element in comparison with the reference [12].

Table 3. The three lowest normalized natural frequencies of the SSSS porous metal foam square plate with a circular hole having varied porosity distributions, coefficients, and length-to-thickness ratio $a/t = 10$

Type	Mode	Porosity coefficient of plate e_0			
		0.1		0.2	
		Pham et al. [12]	ES-MITC3+	Pham et al. [12]	ES-MITC3+
Type I	1	6.4059	6.4114 (0.09%)	6.2905	6.1864 (1.65%)
	2	11.1537	11.1878 (0.31%)	10.9528	10.8355 (1.07%)
	3	11.1545	11.1970 (0.38%)	10.9535	10.8445 (1%)
Type II	1	6.4947	6.3991 (1.47%)	6.4806	6.2839 (3.04%)
	2	11.2808	11.1416 (1.23%)	11.2242	10.9630 (2.33%)
	3	11.2816	11.1506 (1.16%)	11.2250	10.9719 (2.25%)
Type III	1	6.4225	6.3266 (1.49%)	6.3227	6.1286 (3.07%)
	2	11.1778	11.0293 (1.33%)	11.0002	10.7207 (2.54%)
	3	11.1786	11.0382 (1.26%)	11.0010	10.7294 (2.47%)

Table 4. The three lowest normalized natural frequencies of the SSSS porous metal foam square plate with a circular hole having varied porosity distributions, coefficients, and length-to-thickness ratio $a/t = 30$

Type	Mode	Porosity coefficient of plate e_0			
		0.1		0.2	
		Pham et al. [12]	ES-MITC3+	Pham et al. [12]	ES-MITC3+
Type I	1	0.7354	0.7238 (1.58%)	0.7222	0.6980 (3.35%)
	2	1.3753	1.3398 (2.58%)	1.3505	1.2934 (4.23%)
	3	1.3769	1.3408 (2.62%)	1.3521	1.2944 (4.27%)
Type II	1	0.7463	0.7331 (1.77%)	0.7454	0.7193 (3.5%)
	2	1.3946	1.3562 (2.75%)	1.3917	1.3314 (4.33%)
	3	1.3961	1.3572 (2.79%)	1.3932	1.3324 (4.36%)
Type III	1	0.7375	0.7244 (1.78%)	0.7261	0.7008 (3.48%)
	2	1.3789	1.3406 (2.78%)	1.3575	1.2981 (4.38%)
	3	1.3805	1.3416 (2.82%)	1.3591	1.2991 (4.41%)

Table 5. The three lowest normalized natural frequencies of the CCCC porous metal foam square plate with a circular hole having varied porosity distributions, coefficients, and length-to-thickness ratio $a/t = 10$

Type	Mode	0.1		0.2	
		Pham et al. [12]	ES-MITC3+	Pham et al. [12]	ES-MITC3+
Type I	1	14.6715	14.7269 (0.38%)	14.4072	14.2908 (0.81%)
	2	17.6638	17.7442 (0.46%)	17.3456	17.2518 (0.54%)
	3	17.7019	17.7608 (0.33%)	17.3830	17.2680 (0.66%)
Type II	1	14.8251	14.6471 (1.2%)	14.7346	14.4261 (2.09%)
	2	17.8274	17.6364 (1.07%)	17.6939	17.3875 (1.73%)
	3	17.8660	17.6526 (1.19%)	17.7325	17.4036 (1.85%)
Type III	1	14.7009	14.5081 (1.31%)	14.4655	14.1249 (2.35%)
	2	17.6955	17.4800 (1.22%)	17.4091	17.0474 (2.08%)
	3	17.7337	17.4961 (1.34%)	17.4468	17.0632 (2.2%)

Table 6. The three lowest normalized natural frequencies of the CCCC porous metal foam square plate with a circular hole having varied porosity distributions, coefficients, and length-to-thickness ratio $a/t = 30$

Type	Mode	Porosity coefficient of plate e_0			
		0.1		0.2	
		Pham et al. [12]	ES-MITC3+	Pham et al. [12]	ES-MITC3+
Type I	1	1.8366	1.8003 (1.98%)	1.8035	1.7380 (3.63%)
	2	2.3088	2.2463 (2.71%)	2.2672	2.1702 (4.28%)
	3	2.3145	2.2486 (2.85%)	2.2728	2.1723 (4.42%)
Type II	1	1.8625	1.8213 (2.21%)	1.8591	1.7881 (3.82%)
	2	2.3401	2.2716 (2.93%)	2.3343	2.2311 (4.42%)
	3	2.3459	2.2738 (3.07%)	2.3401	2.2333 (4.57%)
Type III	1	1.8414	1.8004 (2.23%)	1.8129	1.7434 (3.83%)
	2	2.3147	2.2461 (2.96%)	2.2786	2.1765 (4.48%)
	3	2.3204	2.2483 (3.11%)	2.2843	2.1786 (4.63%)

In addition, Fig. 13 illustrates the first three mode shapes of the SSSS square plate $a/t = 30$ with a circular hole having the asymmetric porosity distribution $e_0 = 0.1$.

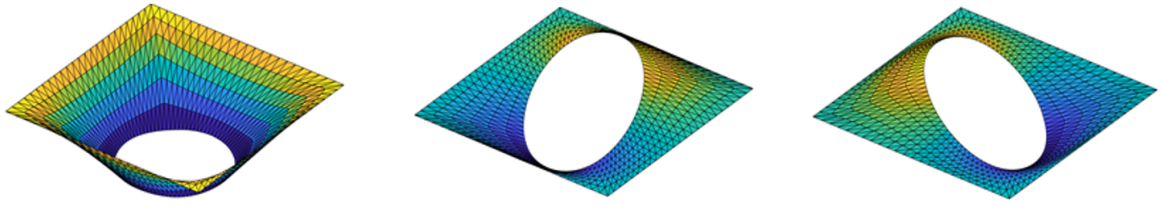

(a) Mode 1 (b) Mode 2 (c) Mode 3

Figure 13. The lowest three mode shapes of the SSSS asymmetrically porous metal foam square plate with a circular hole ($a/t = 30$, $e_0 = 0.1$)

3.2. *Buckling analysis*

Consider a SSSS square plate subjected to uniaxial or biaxial compressions. The plate has the edge a, thickness t and is made of the porous metal foam with the material properties $E_1 = 200$ MPa and $\nu = 0.33$. To compare with the references, the critical buckling load N_{cr} of the plate is normalized by $\overline{N_{cr}} = N_{cr}a^2/\left(E_1 t^3\right)$.

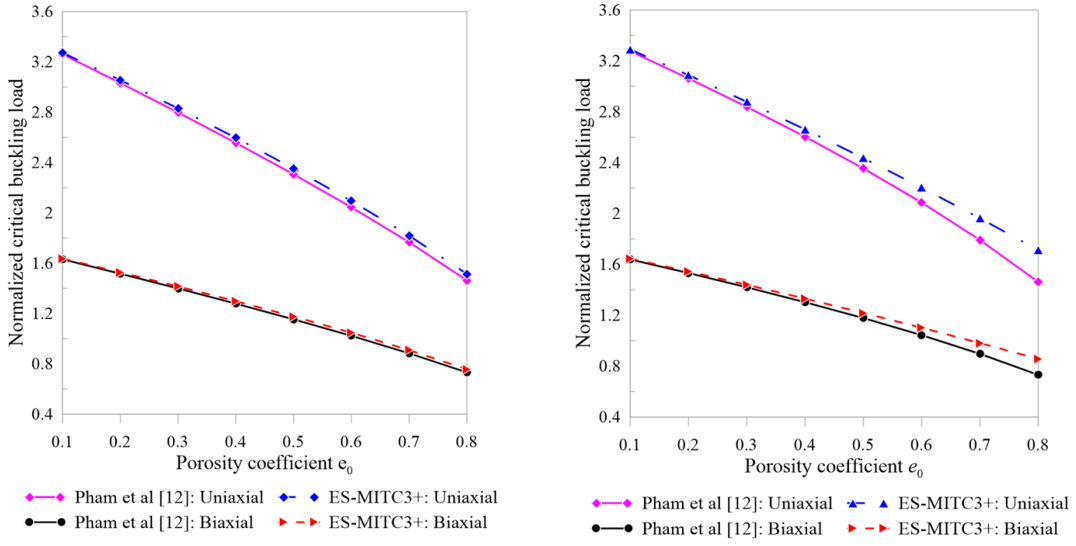

(a) Type I (b) Type III

Figure 14. Critical buckling loads of the SSSS metal foam square plate with $a/t = 10$ under uniaxial and biaxial compressions

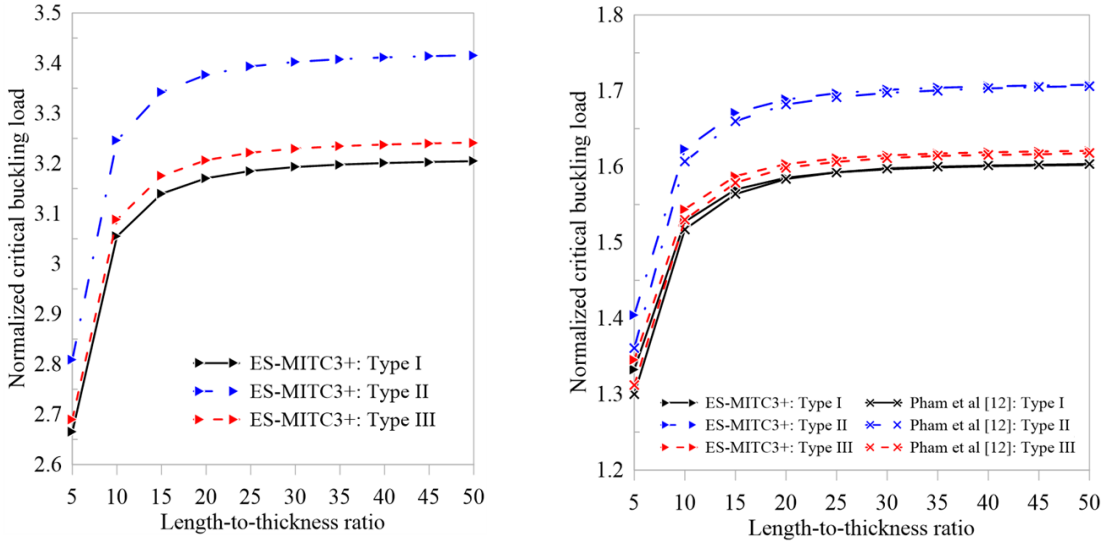

(a) Uniaxial compression (b) Biaxial compression

Figure 15. Normalized critical buckling load of the SSSS metal foam square plate subjected to (a) uniaxial and (b) biaxial compressions in cases of $e_0 = 0.2$ and various length-to-thickness ratios a/t

The plate is discretized by the regular mesh of $N = 24$. For the $a/t = 10$, the effect of the porosity coefficient e_0 on the buckling load of the plate under uniaxial and biaxial compressions given by the ES-MITC3+ element is demonstrated in Fig. 14(a) and Fig. 14(b) for the porous distributions of Type I and Type III, respectively. In both cases of the uniform and asymmetric porosity distributions, Fig. 14 shows that the normalized critical buckling load closely matches to that provided by the reference solution [12].

With the porous coefficient $e_0 = 0.2$, the influence of the length-to-thickness ratios on the normalized critical buckling load of the SSSS metal foam plates having the porosity distributions of Type I, II, III is displayed in Fig. 15(a) and Fig. 15(b) for the uniaxial and biaxial compressions, respectively. Fig. 15(b) indicates the good agreement between the results given by the proposed element and the reference solution [12] for all kinds of the porosity distributions. In both cases of buckling, the critical buckling load values are greatest for the symmetric porous distribution and smallest for the uniform porous distribution.

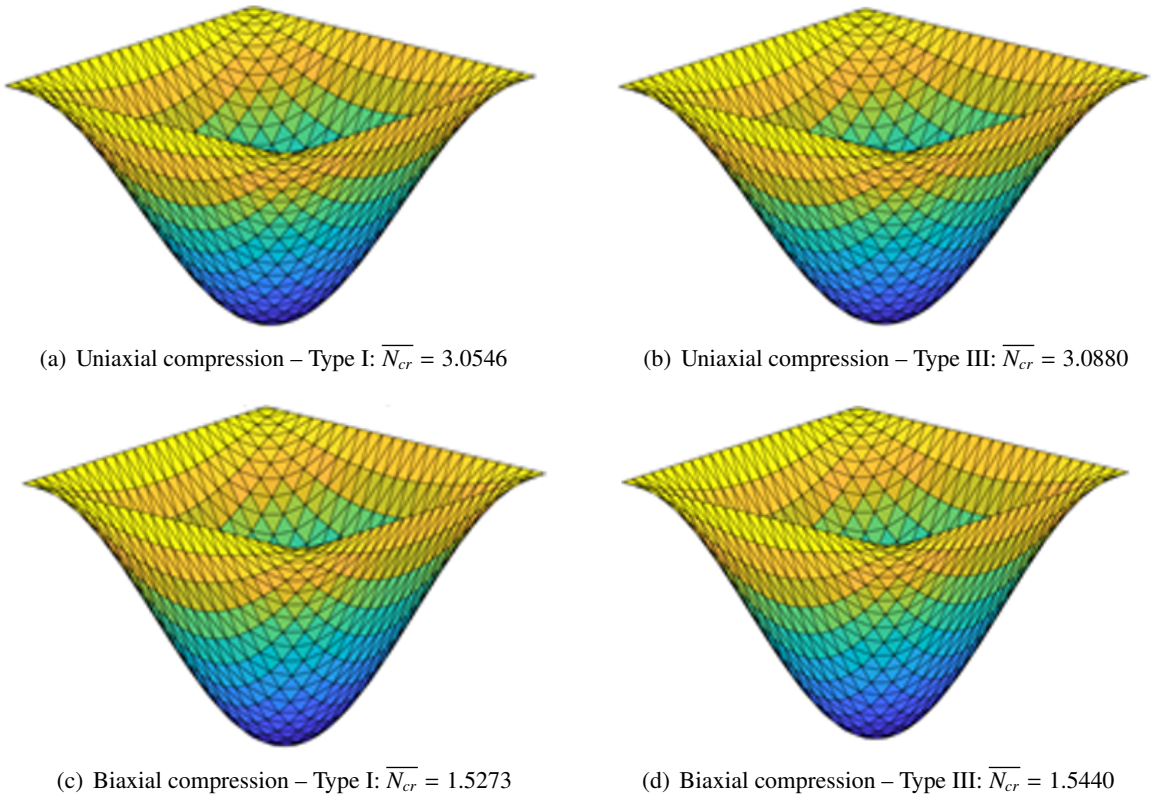

(a) Uniaxial compression – Type I: $\overline{N_{cr}} = 3.0546$

(b) Uniaxial compression – Type III: $\overline{N_{cr}} = 3.0880$

(c) Biaxial compression – Type I: $\overline{N_{cr}} = 1.5273$

(d) Biaxial compression – Type III: $\overline{N_{cr}} = 1.5440$

Figure 16. Mode shape of the buckling load of the SSSS porous metal foam square plate subjected to uniaxial and biaxial compressions with the Type I and Type III porosity distribution in cases of $e_0 = 0.2$ and $a/t = 10$

Furthermore, Fig. 16 shows the mode shape resulting from the buckling load of the SSSS porous metal foam square plate under uniaxial and biaxial compressions in the cases of both uniform (Type I) and asymmetric (Type III) porosity distribution.

4. Conclusions

The study has developed a three-node triangular plate element with the five degrees of freedom per node for the frequency and buckling analysis of porous plates. The displacement approximations

of the proposed element are enriched by the cubic shape function corresponding to the bubble node located at the element centroid. The edge-based smoothed strain method is employed to improve the in-plane strain fields. By using the MITC3+ technique the shear-locking phenomena is eliminated. Based on the first-order shear deformation theory, the ability of the suggested ES-MITC3+ plate element to analyze the frequencies and buckling is evaluated through several plates having different porosity distributions and boundary conditions. Numerical results have shown that the accuracy and convergence of the ES-MITC3+ element well agree with those of reference solutions.

Acknowledgement

This work belongs to the project in 2024 funded by Ho Chi Minh City University of Technology and Education, Vietnam.

References

[1] Liu, P., Chen, G.-F. (2014). *Porous materials: processing and applications*. Elsevier.
[2] Gibson, L. J. (2003). Cellular Solids. *MRS Bulletin*, 28(4):270–274.
[3] Ashby, M. F., Evans, A., Fleck, N. A., Gibson, L. J., Hutchinson, J. W., Wadley, H. N. G., Delale, F. (2001). Metal Foams: A Design Guide. *Applied Mechanics Reviews*, 54(6):B105–B106.
[4] Banhart, J. (2001). Manufacture, characterisation and application of cellular metals and metal foams. *Progress in Materials Science*, 46(6):559–632.
[5] Barati, M. R., Shahverdi, H., Zenkour, A. M. (2016). Electro-mechanical vibration of smart piezoelectric FG plates with porosities according to a refined four-variable theory. *Mechanics of Advanced Materials and Structures*, 24(12):987–998.
[6] Barati, M. R., Sadr, M. H., Zenkour, A. M. (2016). Buckling analysis of higher order graded smart piezoelectric plates with porosities resting on elastic foundation. *International Journal of Mechanical Sciences*, 117:309–320.
[7] Wang, Y. Q., Zhang, Z. Y. (2019). Bending and buckling of three-dimensional graphene foam plates. *Results in Physics*, 13:102136.
[8] Wang, Y. Q., Zu, J. W. (2017). Porosity-dependent nonlinear forced vibration analysis of functionally graded piezoelectric smart material plates. *Smart Materials and Structures*, 26(10):105014.
[9] Tu, T. M., Hoa, L. K., Hung, D. X., Hai, L. T. (2018). Nonlinear buckling and post-buckling analysis of imperfect porous plates under mechanical loads. *Journal of Sandwich Structures & Materials*, 22(6): 1910–1930.
[10] Magnucka-Blandzi, E. (2011). Mathematical modelling of a rectangular sandwich plate with a metal foam core. *Journal of Theoretical and Applied Mechanics*, 49(2):439–455.
[11] Du, Y., Wang, S., Sun, L., Shan, Y. (2019). Free Vibration of Rectangular Plates with Porosity Distributions under Complex Boundary Constraints. *Shock and Vibration*, 2019:1–16.
[12] Hung, P. T., Thai, C. H., Phung-Van, P. (2022). A moving Kriging meshfree approach for free vibration and buckling analyses of porous metal foam plates. *Journal of Micromechanics and Molecular Physics*, 08(01):45–59.
[13] Ebrahimi, F., Habibi, S. (2016). Deflection and vibration analysis of higher-order shear deformable compositionally graded porous plate. *Steel and Composite Structures*, 20(1):205–225.
[14] Rezaei, A. S., Saidi, A. R., Abrishamdari, M., Mohammadi, M. H. P. (2017). Natural frequencies of functionally graded plates with porosities via a simple four variable plate theory: An analytical approach. *Thin-Walled Structures*, 120:366–377.
[15] Lee, Y., Lee, P.-S., Bathe, K.-J. (2014). The MITC3+ shell element and its performance. *Computers & Structures*, 138:12–23.
[16] Liu, G.-R., Trung, N. (2016). *Smoothed finite element methods*. CRC Press.
[17] Thanh, C. D., Chon, T. V., Lan, T. T. H. (2019). An edge-based smoothed MITC3+ element for static analysis of Reissner-Mindlin plates. *Journal of Science and Technology in Civil Engineering (STCE) - HUCE*, 13(4V):139–150. (in Vietnamese).

[18] Chau-Dinh, T., Nguyen, T.-K., Nguyen-Van, H., Ton-That, H. L. (2020). A MITC3+ element improved by edge-based smoothed strains for analyses of laminated composite plates using the higher-order shear deformation theory. *Acta Mechanica*, 232(2):389–422.

[19] Chau-Dinh, T., Tran-Ngoc-Diem, H., Kim, J.-G. (2020). Static Analysis of HSDT-Based FGM Plates Using ES-MITC3+ Elements. In *Computational Intelligence Methods for Green Technology and Sustainable Development*, Springer International Publishing, 375–387.

[20] Barati, M. R. (2017). Nonlocal-strain gradient forced vibration analysis of metal foam nanoplates with uniform and graded porosities. *Advances in Nano Research*, 5(4):393.

[21] Lyly, M., Stenberg, R., Vihinen, T. (1993). A stable bilinear element for the Reissner-Mindlin plate model. *Computer Methods in Applied Mechanics and Engineering*, 110(3–4):343–357.

[22] Rezaei, A. S., Saidi, A. R. (2016). Application of Carrera Unified Formulation to study the effect of porosity on natural frequencies of thick porous–cellular plates. *Composites Part B: Engineering*, 91: 361–370.

[23] Thang, P. T., Nguyen-Thoi, T., Lee, D., Kang, J., Lee, J. (2018). Elastic buckling and free vibration analyses of porous-cellular plates with uniform and non-uniform porosity distributions. *Aerospace Science and Technology*, 79:278–287.